Revision 2

Title: High-pressure spectroscopic study of siderite ($FeCO_3$) with focus on spin crossover

Authors and affiliation:

Cerantola Valerio,[1,*] McCammon Catherine,[1] Kupenko Ilya,[1,2] Kantor Innokentiy,[2] Marini Carlo,[2] Wilke Max,[3] Ismailova Leyla,[1] Solopova Natalia,[1] Chumakov Aleksandr I.,[2] Pascarelli Sakura,[2] and Dubrovinsky Leonid[1]

[1] Bayerisches Geoinstitut, Universitat Bayreuth, D-95440 Bayreuth, Germany

[2] European Synchrotron Radiation Facility, 38043 Grenoble, France

[3] Deutsch GeoForschungsZentrum GFZ, D-14473 Potsdam, Germany

Corresponding Author: Valerio Cerantola, M.Sc. valerio.cerantola@gmail.com

Abstract:

Fe-bearing carbonates have been proposed as possible candidate host minerals for carbon inside the Earth's interior and hence their spectroscopic properties can provide constraints on the deep carbon cycle. Here we investigate high-pressure spin crossover in synthetic $FeCO_3$ (siderite) using a combination of Mössbauer, Raman and X-Ray Absorption Near Edge Structure spectroscopy in diamond anvil cells. These techniques sensitive to the short-range atomic environment show that at room temperature and under quasi-hydrostatic conditions, spin crossover in siderite takes place over a broad pressure range, between 40 and 47 GPa, in contrast to previous X-Ray diffraction data that described the transition as a sharp volume collapse at approximately 43 GPa. Based on these observations we consider electron spin pairing in siderite to be a dynamic process, where Fe atoms can be either high spin or low spin in the crossover region. Mode Grüneisen parameters extracted from Raman spectra collected at pressures below and above spin crossover show a drastic change in stiffness of the Fe-O octahedra after the transition, where they become more compact and hence less compressible. Mössbauer experiments performed on siderite single crystals as well as powder samples demonstrate the effect of differential stress on the local structure of siderite Fe atoms in a diamond anvil cell. Differences in

quadrupole splitting values between powder and single crystals show that local distortions of the Fe site in powder samples cause spin crossover to start at higher pressure and broaden the spin crossover pressure range.

Keywords: siderite, carbonate, deep carbon cycle, spin transition, diamond anvil cell, Mössbauer spectroscopy, Raman spectroscopy, XANES, differential stress

Body of the paper

Introduction

Chemical and physical interactions between atmosphere, biosphere and geosphere are well known and established processes on our planet. However, the mechanisms governing the dynamics and the stability of materials in the deep Earth's interior are still the subject of ongoing debate. The possibility of carbon cycling through the deep Earth (e.g., Dasgupta and Hirschmann, 2010) is demonstrated by observations such as the occurrence of diamonds from the lower mantle, carbonate inclusions in mantle xenoliths and diamonds, and the presence of CO_2 in gases from volcanic eruptions (e.g., Brenker et al., 2007; Harte, 2011; Walter et al., 2011). However, the size of the carbon reservoir inside the Earth is still not well constrained, and is closely linked to the nature of the dominant carrier(s) of carbon down to the core-mantle boundary (e.g., Biellmann et al., 1993; Lavina et al., 2009; Stagno et al., 2011; Boulard et al., 2011).

Deep carbon is predominantly stored in accessory phases as a consequence of its low solubility in dominant mantle minerals (e.g., Keppler et al., 2003), where these accessory phases include carbonates, diamonds/graphite, methane and carbides, depending on pressure, temperature, and oxygen fugacity. In highly reducing environments (i.e., low oxygen fugacity), the crystalline form of carbon is graphite or diamond. At more oxidizing conditions, carbonates are favored due to the reaction between elemental carbon and oxygen to form $(CO_3)^{2-}$ groups that bond to other cations such as Ca^{2+}, Mg^{2+}, Fe^{2+}, Ni^{2+} and Na^{+} depending on the composition of the original bulk assemblage.

The three major carbonate components in the crust and upper mantle are $CaCO_3$ (calcite), $MgCO_3$ (magnesite), and $FeCO_3$ (siderite). The presence of carbonates in the Earth's interior is related to the subduction process, one of the first steps in cycling carbon through the Earth. The $CaCO_3$-$MgCO_3$-$FeCO_3$ system has been

experimentally investigated at relatively low pressures and moderate temperatures (P < 3.5 GPa, T < 1100° C) since many decades (e.g., Goldsmith et al., 1962; Rosenberg, 1967; Merrill and Bassett, 1975; Franzolin et al., 2011). Low-pressure ternary phase diagrams indicate the formation of extensive solid solutions, with compositions depending on pressure and temperature. Observations from geophysics (e.g., Fukao et al., 2009) and natural samples (e.g., Brenker et al., 2007; Walter et al., 2011) suggest that some subducted slabs penetrate the lower mantle. In this case, carbonates could be stable phases due to the proposed higher oxygen fugacity in the region of the slab. The properties of carbonates are, however, not well understood, and many questions remain open regarding their stability, composition and geophysical properties.

Previous high-pressure studies on the carbonate endmembers $CaCO_3$, $MgCO_3$, and $FeCO_3$ revealed high-pressure phase transitions in all phases (e.g., Ono et al., 2005; Merlini et al., 2012; Biellmann et al., 1993; Isshki et al., 2004). Magnesite shows a structural change at 115 GPa and 2100-2200 K (Isshki et al., 2004), whereas magnesiosiderite experiences a volume collapse of almost 10 % between 40 and 50 GPa at ambient temperature, caused by a high-spin to low-spin (HS-LS) transition of iron (Lavina et al., 2009). Shi et al. (2008) predicted the spin transition of Fe in pure siderite by *ab initio* simulations to be between 15 to 28 GPa, while the first experimental observation was reported by Mattila et al. (2007) to occur at roughly 50 GPa from natural siderite powder using X-ray emission spectroscopy. Lavina et al. (2009) described a sharp volume collapse at 43 GPa from X-ray single crystal diffraction, whereas Farfan et al. (2012) observed spin crossover in a (Mn,Mg)-siderite at 46 GPa using Raman spectroscopy and X-ray single crystal diffraction. Lin et al. (2012) studied $Mg_{0.35}Fe_{0.65}CO_3$ up to 80 GPa at ambient temperature and observed the spin transition at 45 GPa, where their data suggested that the low-spin state has different vibrational and elastic properties compared to the high-spin state. Temperature extends the spin crossover region of magnesiosiderite (Liu et al., 2014). Merlini et al. (2012) postulated that the low-spin state could contribute to the stabilization of Fe-bearing Ca,Mg-carbonate (so-called dolomite-III) above 35 GPa and 2000 K, and Liu et al. (2015) reported an orthorhombic phase of magnesiosiderite above 50 GPa and 1400 K that also appeared to be stabilized by spin crossover. It is therefore clear that iron can play a fundamental role in the behavior of carbonates at high pressure and high temperature.

To elucidate the effect of iron on the behavior of carbonates at high pressure, in particular the nature of spin crossover, we undertook a combined spectroscopic study of the siderite endmember. Nuclear resonance techniques (including Mössbauer spectroscopy) provide a sensitive method to detect the response of Fe atoms to physical changes like spin crossover, and X-ray Absorption Near Edge Structure (XANES) and Raman spectroscopies provide complementary information.

Methodology

Synthesis

Iron oxalate (FeC_2O_4) was used as a starting material to synthesize $FeCO_3$. Commercial FeC_2O_4 from Alfa Aesar was used for ^{57}Fe-unenriched samples, while for ^{57}Fe-enriched samples, iron oxalate was synthesized by chemical reaction of ^{57}Fe metal with acetic acid, forming ^{57}Fe-diacetate precipitate, $^{57}Fe(C_2H_3O_2)_2$. The precipitate was then reacted in the presence of oxalic acid to produce ^{57}Fe-enriched iron oxalate. All chemical reactions were run under argon to prevent oxidation of iron to Fe^{3+} at ambient conditions. FeC_2O_4 powder was then sealed in gold capsules of 2.3 mm outer diameter and loaded into an externally heated cold seal vessel and run at 2 kbars and 360 °C for seven days, following French (1971). The obtained powder was used to grow $FeCO_3$ single crystals using a multi-anvil press at Bayerisches Geoinstitut. The powder was pressed inside Re capsules to avoid loss of Fe and placed inside assemblies with $LaCrO_3$ heaters where temperature was measured using $W_{75}Re_{25}/W_{97}Re_3$ thermocouples. The samples were annealed for 10 minutes at 18 GPa and 1600 °C, which yielded single crystals of approximately 5 to 50 μm diameter. The same procedure was used to synthesize both ^{57}Fe-enriched (96% ^{57}Fe) and unenriched (2% ^{57}Fe) $FeCO_3$ single crystals.

High pressure experiments

Diamond anvil cells (DACs), type BX-90 (Kantor et al., 2012), were mounted with diamonds with culet sizes of 250 μm and rhenium gaskets with 120 μm starting diameter hole were employed in all experiments. We used neon gas loaded under pressure (1.4 kbar) (Kurnosov et al., 2008) as a pressure-transmitting medium to obtain hydrostatic conditions, and we measured the wavelength of the ruby fluorescence before and after each experimental run to calculate pressure (Mao et al., 1986). The difference in values contributed to the pressure uncertainty, which was

estimated to be 1 and 3 GPa for single crystal and powder experiments, respectively. All DACs were prepared by loading a ~ 15 - 20 μm diameter isomeric $FeCO_3$ single-crystal chip and a smaller ruby crystal (Fig. 1a), with the exception of Mössbauer measurements using a radioactive source where more than ten ^{57}Fe-enriched crystals were used in the pressure chamber to optimize signal acquisition time and signal to noise ratio (Fig. 1b). A similar series of Mössbauer measurements was also performed using $FeCO_3$ powder, which was compressed to a pellet before loading in the DAC in order to reduce porosity between the grains. All single crystals survived intact throughout each experimental run without breaking or cracking. To test the degree of hydrostaticity, in some experiments we placed two or three ruby crystals in different positions inside the pressure chamber. In all cases we measured the pressure from each ruby within the same experiment to be within ± 1 GPa of each other.

In situ **analytical techniques**

Mössbauer spectroscopy

^{57}Fe Mössbauer spectra were recorded at room temperature in transmission mode on a constant acceleration Mössbauer spectrometer with a nominal 370 MBq ^{57}Co high specific activity source in a 12 μm-thick Rh matrix (referred to below as "in house" spectra). Spectra collection took 2 to 4 days for each pressure point. A set of Mössbauer spectra was also collected during compression using the Synchrotron Mössbauer Source (SMS) at the European Synchrotron Radiation Facility (ESRF), Grenoble, France on the Nuclear Resonance beamline (Rüffer et al., 1996) ID18. The narrow (~6 neV) energy component of X-rays at the Mössbauer energy of 14.4 keV was extracted from a wide spectrum of synchrotron radiation using a $^{57}FeBO_3$ single crystal monochromator and focused to a beam width of size of 10x15 μm^2 using Kirkpatrick-Baez mirrors (Potapkin et al., 2012). Each SMS spectrum took approximately thirty minutes to collect. The velocity scales of all Mössbauer spectra were calibrated relative to 25 μm thick α-Fe foil, and all spectra were fitted using the software package MossA (Prescher et al., 2012a). All Mössbauer measurements were performed on ^{57}Fe-enriched $FeCO_3$.

Raman spectroscopy

Raman measurements were performed on a DILOR XY triple spectrometer using the 514 nm line of Ar^+ laser with 2 cm^{-1} spectral resolution and 2 μm spatial resolution at 300 mW of power. Data acquisition was performed with a frequency range extending from 150 to 1300 cm^{-1}. In order to maximize the signal to noise ratio, each spectrum was collected in three steps over three smaller regions of frequency, where each region was measured five times using an exposure time of 60 seconds, and then merged together at the end of the acquisition. Orientation effects of the single crystals and hence any polarization effects on the spectra are considered to be negligible since we used an unpolarized green Raman source and all crystals were maintained in the same orientation during the experiment. All Raman data presented in the paper were collected on the same single crystal up to the target pressure. Raman measurements were performed at Bayerisches Geoinstitut, Bayreuth, Germany, and spectral fitting was carried out using the software package PeakFit (Systat Software).

XANES spectroscopy

Fe K-edge XANES measurements were performed at ESRF at the energy dispersive X-ray absorption spectroscopy (XAS) beamline ID24 (e.g., Pascarelli et al., 2006). The beam was focused horizontally using a curved polychromator Si 111 crystal in Bragg geometry and vertically with a bent Si mirror. The obtained cross-section is about 3x5 (HxV) μm^2. The measured XANES spectra were normalized using the Athena software package (Ravel et al., 2005), and the second-order polynomial for the pixel to energy conversion parameters was calibrated using a reference α-Fe foil spectrum.

Results

Mössbauer spectroscopy

Mössbauer spectroscopy provides information about the electronic, magnetic and structural properties of specific elements within a material. The extremely narrow line width of gamma rays (4.5×10^{-9} eV in the case of ^{57}Fe) provides Mössbauer spectroscopy with the sensitivity to detect spin transitions in compounds with Mössbauer-active nuclei.

The evolution of $FeCO_3$ Mössbauer spectra at 298 K and increasing pressure is similar to spectra already reported for other non-magnetic compounds containing Fe^{2+} in an octahedral environment, for example ferropericlase (Fe,MgO) (Kantor et al.,

2006b). At pressures below 40 GPa, Fe^{2+} in octahedral coordination is represented by a doublet, while at higher pressures the doublet is progressively replaced by a singlet, which at pressures higher than 45 GPa is the only component present in the spectra of single-crystal $FeCO_3$ (Fig. 2a, 2b). Mössbauer spectra of powder $FeCO_3$ show a similar evolution with increasing pressure, but over a larger pressure interval (Fig. 2c).

The centre shift (CS) is sensitive to the s-electron density at the nucleus, while the quadrupole splitting (QS) measures the electric field gradient (EFG) caused by a non-symmetrical charge distribution around the nucleus. The evolution of hyperfine parameters with increasing pressure for both single crystals and powder samples is shown for CS and QS in Figs. 3a and 3b, respectively. The general trend of the CS of is to decrease with increasing pressure, where the CS of the singlet is approximately 0.3 mm/s lower than the CS for the doublet (Fig. 3a). The behavior of the CS is similar for single crystals and powder; however for the QS the behavior differs, which will be discussed in more detail below. Here we just mention that the QS of the doublet for single crystals remains essentially constant with increasing pressure with a slight decrease just before the singlet appears at 45 GPa.

Mössbauer spectra of $FeCO_3$ single crystals collected in house and using the SMS are slightly different. Each SMS spectrum shows significantly higher resonant absorption and unequal areas of doublet components compared to spectra collected using a radioactive source (Fig. 4). Both of these features are due to properties of the synchrotron X-ray source, namely the low amount of non-resonant radiation and the polarization of the source, which leads to selective excitations of nuclear levels. However all hyperfine parameters of single crystal spectra are the same within experimental uncertainty (Figs. 2, 3, 5), hence SMS and in house spectra can be used interchangeably for interpreting hyperfine parameter variations. In contrast there are significant differences between in house spectra of single crystal and powder $FeCO_3$, including the linewidths (Fig. 5), which will be discussed below in the context of the effect of stress in DACs.

Raman Spectroscopy

Raman spectroscopy provides direct insight into the vibrational behavior of ions or groups of ions bonded together, such as $(CO_3)^{2-}$, and their variation as a response to changes of external parameters such as pressure and temperature. In $FeCO_3$, $(CO_3)^{2-}$

groups form planes perpendicular to the *c* axis with Fe occupying the interstitial space between them to form octahedral sites coordinated by oxygen atoms. This structural arrangement is typical for carbonates and is known as the calcite or magnesite-type structure. For symmetry reasons (e.g., Rutt and Nicola 1974) the cations give rise to modes that are Raman inactive. Hence, typical Raman spectra of calcite-type carbonates show mainly external and internal vibrations due to the motion of $(CO_3)^{2-}$ ions.

At ambient conditions carbonate spectra show six Raman bands in the region from 200 to 1800 cm^{-1}. However, above 1300 cm^{-1} only two bands are detected and correspond to weak asymmetric stretching vibrations of $(CO_3)^{2-}$. We neglect these bands to avoid the signal from the diamonds and focus on frequencies below 1300 cm^{-1}. In this region the $FeCO_3$ Raman spectrum has four vibrational modes (176, 274, 728 and 1077 cm^{-1}) (Fig. 6). Based on previous studies (Popkov et al., 1973, Rutt and Nicola, 1974) we assign the two lower frequency lines to external E_g modes that are translations between cation and anion groups and the two higher frequency lines to internal modes, E_g and A_{1g}, that are caused by symmetric bending and stretching of $(CO_3)^{2-}$, respectively. A broad low intensity peak was also observed in the region around 500 cm^{-1}, which is attributed to electronic Raman scattering from the Fe^{2+} ion (Rutt and Nicola, 1974). However, the peak is only visible at ambient conditions and is too weak to be observed at higher pressures.

All bands shift to higher frequencies with increasing pressure up to 40 GPa, but at slightly higher pressure there is a clear change in the behavior of Raman modes (Fig. 6 and 7). The A_{1g} mode splits with the growth of a second peak at slightly lower frequencies. With increasing pressure the new Raman band becomes progressively more intense, growing at the expense of the higher frequency peak until the latter completely disappears between 47 and 50 GPa. The internal E_g line jumps discontinuously to higher wavenumbers (from 782 to 840 cm^{-1}) at roughly 43 GPa, and a broad hump emerges at 755 cm^{-1}, which might also be attributed to the electronic Raman scattering of the Fe^{2+} ions at high pressures. The external E_g vibrations are also affected by the transition. The E_g vibrational mode at 289 cm^{-1} completely disappears after 45 GPa, while the higher frequency external E_g vibration shifts from 449 cm^{-1} to 543 cm^{-1} between 43 and 45 GPa (Figs. 6 and 7). Above 47 GPa and up to 58 GPa, the highest pressure reached by Raman spectroscopy, the new

HP Raman modes continue to shift to higher frequencies, although with lower slopes than observed at pressures below the transition.

Normalized spectral intensities highlight the progressive decrease of intensity of lower frequency bands between 0 and 40 GPa (Fig. 8). At higher pressures (> 45 GPa) the high frequency external and internal E_g modes, which are weak and difficult to distinguish in spectra near the transition pressure, gradually become more intense.

XANES spectroscopy

X-ray Absorption Fine Structure (XAFS) spectroscopy is an element-specific method to study the local atomic structure within a material. XAFS spectra can be divided into different regions based on the energy range from the absorption edge in the spectrum. Our study focuses on the XANES region, which is generally taken to extend 50 eV beyond the edge itself.

Fig. 9 shows normalized XANES spectra of $FeCO_3$ collected during compression. The 1 bar spectrum is consistent with the data of Wilke et al. (2001), although the pre-edge peak is less pronounced in our study due to differences in energy resolution. Each spectrum is characterized by two peaks (identified in Fig. 9 as "1" and "2") below 7150 eV. Their relative intensities change at increasing pressure and their positions shift to higher energies (Fig. 10). Peak shifts of the main-edge energy on compression was already observed in previous studies on ferropericlase (Kantor et al., 2006a; Narygina et al., 2009) and bridgmanite (Narygina et al., 2009) and is related to changes in the electronic structure due to shortening of Fe-O distances. This shortening is directly reflected in the shift of the first EXAFS maximum between 7160 and 7180 eV to higher energy, which may be described by the relation $\Delta E \times R^2 = \text{const.}$ (e.g.,Bianconi et al., 1983, Wilke et al., 2007), where ΔE is the energy difference between the onset of the edge and the first EXAFS maximum and R is the Fe-O distance.

All peaks change strongly between 40 and 44 GPa, where the pre-edge region shows the largest variation (Fig. 9a and 10). The pre-edge peak at ~ 7112 eV, which is not well resolved in this dataset, becomes more intense and sharper above 44 GPa (Fig. 9b). At ~ 7117 eV, ~ 5 eV higher than the pre-edge, a shoulder present at lower pressure evolves into a better-resolved feature, so that it appears like an additional pre-edge. The grey dashed area in Fig. 10 marks the energy where the appearance of this feature is observed, matching the discontinuity in the trends of the main and pre-

edge peaks. Similarly, the main-edge region (7120-7140 eV) shows considerable changes between 40 and 44 GPa. The intensities of the main peaks are reversed for spectra above 40 GPa, where the second peak becomes more intense than the first (Figs. 9 and 12). Additionally, all spectra above 44 GPa show the presence of a new pronounced feature, identified as "3" in Fig. 9.

The derivative $\delta\mu/\delta E$ provides a more sensitive probe of changes in the spectra (Fig. 11). The grey arrows together with the dashed lines highlight three features that are related to the changes observed in the spectra: 1) the derivative maximum at ~ 7115 eV that disappears below 44 GPa and is substituted by another maximum at ~ 7117 eV; 2) a shoulder at ~ 7128 eV that appears above 44 GPa and sharpens on further increase of pressure to 51.5 GPa; 3) the derivative minimum at ~ 7150 eV that appears above 44 GPa. These changes in the pre-edge, XANES and low-energy EXAFS regions imply modification of the local structure around Fe atoms and/or chemical bonding between 40 and 44 GPa.

The intensity ratio of the two peaks at the main edge, I_1/I_2, provides another qualitative probe of changes in the local structure. The intensity ratio decreases monotonously until 40 GPa, where it then sharply decreases by 18.5 % in one step to 44 GPa (Fig. 12). Above 44 GPa the intensity ratio does not vary significantly with pressure up to 51.5 GPa, the highest pressure reached.

Discussion

Spin transition

Changes observed in the Mössbauer, Raman and XANES spectra of $FeCO_3$ that take place between ~ 40 and 45 GPa (or 47 GPa according to Raman data) result from electronic spin crossover of *3d* electrons of Fe^{2+} atoms. Mössbauer spectra of single crystal $FeCO_3$ show decreasing values of CS with increasing pressure up to 40 GPa that can be explained by increasing *s* electron density at the Fe nucleus due to the progressive reduction of interatomic distances. The new component that appears at 40 GPa has zero QS and a CS that is much smaller than the HS component, similar to LS Fe^{2+} in ferropericlase and bridgmanite (e.g., Kantor, 2007, McCammon et al., 2010). LS Fe^{2+} in octahedral coordination has no unpaired electrons with nearly spherical charge distribution; hence the EFG is essentially zero because all 3*d* energy levels are nearly equally occupied. Spin pairing changes abruptly the degree to which *s*-electron density at the Fe nuclei is shielded by 3*d* electrons; hence the CS drops considerably.

The decrease in CS at the transition is roughly 0.3 mm/s, which is higher than the value observed for ferropericlase (~ 0.17 mm/s, Kantor 2007), but lower than for iron-organic complexes (~0.5 mm/s, Gütlich et al., 1978) at ambient or low (< 5 GPa) pressure.

Raman spectroscopy also provides evidence of the spin transition in $FeCO_3$, but through the interatomic vibrations in the sample that are probed by inelastic scattering of light. Unit cell compression between 1 bar and 40 GPa causes a shift of the Raman bands to higher frequencies, to a first approximation following eq. (1):

$$v = \frac{1}{2\pi}\sqrt{\frac{F_r}{\mu}} \qquad (1)$$

where v is the frequency, F_r is the restoring force and μ is the weighted mass of the molecule or group of atoms.

Between 40 and 47 GPa the A_{1g} mode shifts abruptly to lower frequency, comparable to observations by Farfan et al. (2012) and Lin et al. (2012) for natural siderite enriched in manganese and magnesium, respectively. The A_{1g} mode is attributed to the internal stretching vibration of the carbonate groups. It is therefore strongly dependent on the distance between C and O, and its frequency will decrease with increasing distance. The shift to lower frequency is thus a clear sign of an increase of the C-O distance. This interpretation is consistent with observations by Lavina et al. (2010a), who observed an increase in the C-O bond length in natural siderite at 43 GPa and attributed it to structural re-organization caused by spin pairing of Fe^{2+} atoms, where shared oxygen atoms that are shared by CO_3-groups and Fe^{2+} are displaced due to the volume collapse of the octahedral site. In contrast, we observed a frequency increase of the external and internal E_g bands at the spin transition. The external modes, which in $FeCO_3$ are translational modes between the anion $(CO_3)^{2-}$ and cation (octahedral Fe^{2+} coordinated by oxygen) sites, are clearly influenced by the volume collapse of Fe-O octahedra at the transition. The distances between carbonate groups and cations become shorter; hence the frequency increases. The internal E_g mode, which is caused by in-plane symmetric bending of the carbonate molecule, shifts to higher frequency due to the systematic decrease in the O-O bond length after the transition (Lavina et al., 2010a), which induces higher vibrational frequencies due to the decrease of the atomic distance between neighboring oxygen atoms.

Both Mössbauer and Raman data highlight an important point regarding spin pairing in $FeCO_3$: under quasi-hydrostatic conditions the process occurs over a pressure interval of at least 5 GPa (Figs. 2, 6, 7 and 9). The integrated area of the two components in the Mössbauer spectra and the two A_{1g} bands in Raman spectra allow the percentage of iron atoms in the HS and LS states to be estimated. From Mössbauer spectra at 41 GPa, 12% of Fe^{2+} atoms are in the LS state. This observation suggests that the proportion of Fe atoms changing to the LS state does affect the local symmetry and hence the position of the surrounding atoms, inducing short-range (on the Ångstrom scale) local "structural relaxation" that broadens the transition pressure range. Indeed, since there is a mixture of Fe atoms in HS and LS in the transition region that progressively change to LS, a local structural relaxation that results in stretched bonds between Fe and O will enable some Fe atoms to persist in the HS state over a broader pressure range, being less compressed by the surrounding oxygen atoms.

While a detailed quantitative analysis of XANES spectra incorporating *ab initio* simulation is beyond the scope of this study, our XANES data can be used to investigate the degree to which spin crossover in $FeCO_3$ can be detected qualitatively, and how well changes in the local structure can be derived from empirical analysis of the spectra.

The most striking change in the pre-edge region is the abrupt appearance of an additional peak at 7117 eV at 44 GPa. This feature shifted from higher energy, where it was present only as a shoulder in the onset of the main edge. This feature is related to excitations of 1*s* to 4*p* electron states of the valence band (e.g., Caliebe et al., 1997), which shift to lower energy with decreasing Fe-O distance. In the actual pre-edge region at ~ 7112 eV which is related to *1s* → *3d* transitions, a change from a doublet feature for HS to a singlet in LS is expected as shown by Westre et al. (1997) by experiment and multiplet analysis on octahedral high and low spin complexes. The quality of the data shown here is insufficient for a detailed analysis of the pre-edge due to limited energy resolution and a high level of noise. Nevertheless, a detectable "sharpening" of the pre-edge peak between 40 and 48 GPa can be observed as seen in Fig. 9b. Westre et al. (1997) explains the change in the pre-edge region as a change in the accessible electronic states that contribute to the pre-edge after the change in spin state of 3*d* electrons. In the HS state the octahedral crystal field splits the 3*d* electron levels into e_g and t_{2g} states, giving rise to three possible transitions from the 1*s* level.

Two of the levels are close in energy; hence an apparent doublet is observed for octahedral site symmetry (see also Westre et al., 1997, Wilke et al., 2001). In the LS state only the e_g level is unoccupied, so only one transition is possible.

In the energy region of the main edge (7120-7140 eV) the peaks in the spectrum of $FeCO_3$ correspond to a combination of *1s* → *4p* electronic transitions and/or multiple scattering of the photoelectron by neighboring atoms (Fig. 9a, peaks 1 and 2) (Caliebe et al., 1997, Mottana, 2004). The positions of these peaks shift to higher energy from 1 bar to 40 GPa (Fig. 10) due to unit cell compression and the resulting decrease in Fe-O bond length, that is also responsible for the increase in the intensity of peak 2 with increasing pressure. The decrease in intensity is likely related to a decrease in the density of *p*-like states in that energy region as a consequence of changes in bond length. Between 40 and 44 GPa where spin crossover occurs, the spectra show an abrupt change in the relative amplitudes of peaks 1 and 2, the appearance of peak 3 and the sudden shift to higher energies of the first EXAFS oscillation (roughly from 7170 to 7180 eV, see Figs. 9 and 11). Again, these changes are directly related to the collapse of the Fe coordination polyhedron, i.e., the change in Fe-O distance (Wilke et al., 2007, Bianconi et al., 1983). In addition, the appearance of peak 3 above 44 GPa could arise from multiple scattering of the photoelectron from the neighboring O atoms, which move closer to the Fe atoms after the transition.

While a comprehensive quantitative analysis of the spectra in terms of structural changes would require *ab initio* calculations that are beyond the scope of this paper, we may use the relation $\Delta E \times R^2 = \text{const.}$ to estimate the change in the Fe-O distance with pressure from the XANES spectra. To perform this analysis, we use the spectral feature that is located at 7172.5 eV at 0 GPa and define the onset of the edge at the position of the pre-edge (7112 eV) (see also Wilke et al., 2007). This analysis yields $\Delta E_0 = 60.5$ eV at 0 GPa, $\Delta E_{40} = 68.9$ eV at 40 GPa and $\Delta E_{48} = 75$ eV at 48 GPa. Assuming that the constant in the relation given above is independent of pressure, we can write for 0 and 40 GPa:

$$\Delta E_0 \times R_0^2 = \Delta E_{40} \times R_{40}^2, \quad (2)$$

which can be rearranged to

$$(\Delta E_0 / \Delta E_{40})^{0.5} = R_{40} / R_0. \quad (3)$$

From the two values obtained at 0 GPa and 40 GPa, a shortening of the Fe-O distance by a factor of 0.94 is estimated, while across the spin transition from 40 and 48 GPa,

437 we obtain a value of 0.95. This is comparable to the value of 0.92 obtained by Lavina
438 et al. (2010) based on single crystal diffraction data (their Fig. 7). The consistency of
439 results is striking, particularly considering the large simplifications made in our
440 analysis, and highlights the sensitivity of XANES to the local environment.
441 Our results clearly demonstrate the capability of XANES spectra to detect spin
442 crossover in $FeCO_3$. Indeed, the sensitivity has improved markedly since previous
443 studies of other geophysically relevant phases such as ferropericlase (Kantor et al.,
444 2006a) and bridgmanite (Narygina et al., 2009) due to the newly upgraded
445 experimental setup for high-pressure XAFS studies on beamline ID24 at ESRF,
446 together with the implementation of more hydrostatic conditions in the DAC, for
447 example through the use of neon as a quasi-hydrostatic pressure medium. The higher
448 sensitivity could also be related in part to the specific structural arrangement in
449 carbonates (planes of $(CO_3)^{2-}$ alternated by octahedrally coordinated cations).
450 Simulations to quantitatively evaluate the effect of spin crossover on the XAFS
451 spectra are ongoing and will be reported elsewhere.
452
453 *Dynamic spin state distribution*
454 Previous X-ray diffraction (XRD) experiments on siderite and ferromagnesite (e.g.,
455 Lavina et al., 2009, 2010a, Merlini et al., 2012, Lin et al., 2012) interpreted spin
456 crossover to be a relatively sharp discontinuity taking place at roughly 43 GPa and
457 causing a discontinuous volume reduction of the unit cell. Indeed, XRD is a technique
458 sensitive to long-range structures and cannot probe short-range order such as, for
459 example, HS and LS state distributions. Raman, Mössbauer and XANES spectroscopy
460 probe the local structure of neighboring atoms and groups of atoms and are therefore
461 sensitive to short-range order features that are not always evident from XRD. Our
462 results, i.e., a successive change of all spectra from HS to LS across a relatively wide
463 pressure range, support the idea of a dynamic nature of spin crossover, which involves
464 a non-static distribution of HS and LS states until the transition is complete. Indeed, a
465 static distribution of the two spin states, which could be considered as a long-range
466 order feature, should be easily resolved by XRD, but so far it has not been reported.
467 Hence, we propose that if a static distribution of the two spin states can be excluded
468 because it was not observed by XRD, the only way to explain the broad and transient
469 pressure range over which spin crossover takes place is a dynamic distribution of HS
470 and LS states in the transition region. On the basis of our result, we suggest that

previous XRD studies could be re-examined to investigate if certain features (i.e., the peak splitting and diffuse scattering in Lavina et al., 2010a or the small deviation in the low pressure equation of state before the volume collapse in Merlini et al., 2013), could reflect a more complex transition.

A direct consequence of the broad spin crossover pressure range is highlighted by the weakening of all Raman E_g bands as spin crossover is approached, followed by an intensity increase once the final LS state is achieved (Fig. 8). All modes become progressively weaker during compression due to the gradual pressure increase that affects the interaction between the probing laser and the sample, hence reducing signal quality. However, the laser-sample coupling does not explain the almost complete disappearance and reappearance of the lower frequency modes at the transition. Lavina et al. (2009) described a change in the color of the crystals, where they become progressively darker during and after spin pairing. We observed a similar behavior, where crystals changed from a light reddish color to a slightly darker one. Since we used a green laser with 514 nm wavelength one might attribute the decrease in intensity of the Raman bands to a change in phonon scattering in the visible light region. However, we consider this not to be the case since this does not account for the regain in intensity of the other Raman bands after the transition, and also the internal symmetric stretching vibration A_{1g} is not affected. Hence, we attribute these intensity minima (Fig. 6) to static disorder caused by spin pairing through the decreased percentage of atoms scattering in the HS state, and consequently the increased amount of scattering by LS atoms. Once the transition is complete, all atoms/molecules in the LS state scatter again equally based on their different vibrational symmetries and new and more intense modes reappear in the spectra. One mode is completely lost after the transition (the external vibration that occurs at 176 cm^{-1} at 1 bar); however it is the lowest frequency E_g translatory oscillation and might be simply too weak to be detected.

Grüneisen parameters

We calculated the mode Grüneisen parameters (γ_i) for each vibrational mode with increase of pressure using the following equation:

$$\gamma_i = \frac{K}{\omega}\frac{d\omega}{dP} \qquad (4)$$

where the bulk modulus (K) is 117±1 GPa (Zhang and Reeder, 1999) and 148±12 GPa (Lavina et al., 2010) for the HS and LS states, respectively. We also calculated the pressure shift ($d\omega/dP$) in order to verify that the differences in the Grüneisen parameters before and after the spin transition were not caused simply by the use of a different bulk modulus (Table 1).

The Grüneisen parameters of HS $FeCO_3$ discriminate the two different vibration typologies, internal and external, characterized by smaller and larger values, respectively. In both cases our results match the observations of Santillán and Williams (2004) that were based on infrared measurements. Indeed, the Grüneisen parameters reflect the effect that changing the volume of a crystal lattice has on its vibrational properties, in this case due to the increase of pressure. The higher values of the external translatory oscillations are consistent with values reported by Ross and Reeder (1992), who described by means of single-crystal XRD the higher compressibility of Fe-O octahedra with respect to the relative incompressibility of the CO_3 group. Hence, the vibrations associated with the relative translation of the cation with respect to the anionic group are expected to have higher Grüneisen parameters, where the cation site is more affected by the pressure increase due to its higher compressibility.

The Grüneisen parameters measured at spin crossover are also characteristic of the vibrational typology: the internal modes show no variation (A_{1g}) or a moderate increase (E_g) in their values; whereas the remaining external mode (E_g) drops drastically from 1.16 to 0.72, similar to observations by Lin et al. (2012) for ferromagnesite. Indeed at spin pairing the Fe-O octahedra shrink, pulling the oxygen atoms towards the iron atoms and consequently stretching the C-O bonds in the carbonate groups. The external vibration (translatory oscillation) is affected by the shape and the size of the cation site, which is less distorted (Lavina et al., 2010a) and has a smaller volume after the transition due to the more compact environment (lower Grüneisen parameter). On the other hand, the stretching of the C-O bond does not influence the carbonate groups; hence the Grüneisen values for the internal vibrations remain constant for symmetric stretching (A_{1g}) or show a slight increase for symmetric bending (E_g), where the difference is probably related to the different vibrational geometry.

Compared to the study of Lin et al. (2012), we obtain lower values of calculated Grüneisen parameters for both HS and LS states. This may be attributed to the

539 difference in composition and its effect on the bulk modulus, since the latter is the
540 only adjustable parameter used to calculate γ_i (Eq. 4). Indeed, the frequency variation
541 with pressure ($d\omega/dP$) of each mode displays similar values in both studies.
542 Our calculations relate to the mean mode Grüneisen parameter for all observed
543 vibrations in HS and LS states. Since we recognize that not all phonon modes are
544 taken into account, for example all Raman bands above 1300 cm^{-1} are excluded, it is
545 not appropriate to compare it with the thermodynamic Grüneisen parameter (e.g.,
546 Santillán and Williams, 2004, Lin et al., 2012, Liu et al., 2014). Instead our aim is to
547 provide an indication of the difference in compressibility of the $FeCO_3$ structure
548 before and after the transition based only on a limited number of vibrations. From our
549 calculations, the average Grüneisen parameters of HS and LS states are, respectively,
550 0.69 and 0.42. As stated by Lin et al. (2012), the LS state is expected to have a
551 thermodynamic Grüneisen parameter lower than ~1.1, which is the value for the HS
552 state. Our available data suggests the decrease of the Grüneisen parameter to be ~
553 30%, but this should be tested by further experiments.
554
555 **Effect of stress on Mössbauer spectra collected in a DAC**
556 Differences between powder and single crystal Mössbauer spectra of $FeCO_3$ provide
557 information on the effects of deviatoric and local stresses caused by non-hydrostatic
558 conditions. Any DAC, due to its intrinsic geometry, causes cylindrically symmetric
559 non-hydrostatic stress fields during compression that affect all materials with non-
560 zero yield strength (e.g., Meng et al., 1993; Dubrovinsky and Dubrovinskaia, 2004;
561 Kenichi T., 2000; Zhao et al., 2010). For any type of pressure-transmitting medium
562 there is a pressure limit at which hydrostatic behavior of the medium is lost and
563 consequently deviatoric stresses develop within the sample. These stresses are
564 macroscopic when they are caused by the action of the transmitting medium on the
565 sample and microscopic when they develop at the grain boundaries of polycrystalline
566 samples, i.e., powders (Weidner et al., 1994). Observables from Mössbauer
567 experiments provide qualitative insight into the effects of deviatoric stress on the
568 nuclear behavior and spin crossover of Fe atoms in siderite powder in DACs gas-
569 loaded with neon.
570 The observed differences between powder and single crystal Mössbauer spectra
571 arise from the action of microscopic local stresses present at grain boundaries. Indeed,
572 the powder sample was compressed with the intention of producing a pellet with

573 reduced interstitial porosity (20 μm size in diameter), so that Ne was acting more as a
574 lubricant between powder grains than as an effective pressure-transmitting medium.
575 This effect is apparent from the influence of pressure on the FWHM of Mössbauer
576 absorption peaks for powder and single crystals experiments (Fig. 5). With the
577 exception of the 1 bar powder spectrum, all peaks at higher pressures are at least
578 twice as broad for powder compared to single crystals, where the difference increases
579 at higher pressure. The broadening originates from pressure gradients in the gasket
580 hole, which in turn create pressure gradients within the sample. Due to the relatively
581 large cross section of the gamma-ray beam in our laboratory (~ 500 μm) compared to
582 the size of the gasket hole, at each pressure point the resultant Mössbauer spectrum
583 that is measured represents the combination of several spectra collected at slightly
584 higher and lower pressures compared to the pressure measured by ruby fluorescence
585 due to the pressure gradient. In this way spectra characterized by higher and lower CS
586 are merged together and the components in the final spectrum appear broadened.
587 There is little difference in the measured CS of powder and crystals (Fig. 3a), but the
588 differences measured for QS are significant (Fig. 3b). Indeed, the QS values for
589 powder spectra are systematically (except at 1 bar) at least 15% higher than for the
590 single crystal measurements. The physical explanation is straightforward: powder
591 experiments involve grain-grain interactions that develop under compression and
592 cause the formation of deviatoric stress acting on the local structure around the Fe
593 atoms, causing the Fe-O octahedra to be more distorted than in "regular" quasi-
594 hydrostatic experiments. The distortion induces variations in the shape and size of the
595 charge distribution around the Fe nuclei and ultimately on the electric field gradient,
596 hence on the quadrupole splitting.
597 The macroscopic and microscopic stresses that develop inside the gasket hole
598 also influence spin crossover. Important differences between powder and single
599 crystal Mössbauer spectra are: 1) spin crossover starts at lower pressure for single
600 crystals (~ 40 GPa) compared to powder (~ 50 GPa); and 2) the pressure range over
601 which spin crossover occurs is smaller for single crystals (~ 5 GPa) than for powder
602 (> 10 GPa). Moreover, the sudden increase (~ 15 %) of QS in powder spectra at the
603 start of spin crossover is caused by enhanced distortion of Fe octahedra in the crystal
604 structure. Indeed at the spin pairing transition, the dynamic distribution of HS and LS
605 states, with respectively larger and smaller octahedra, unbalances the surrounding

606 atomic distribution, stretching or shortening atomic bonds that favor the formation of
607 local stresses.
608
609 **Implications**
610 On the basis of this study, we found that spectroscopic techniques provide insight into
611 the short-range atomic order during $FeCO_3$ compression from 1 bar to 58 GPa. In
612 addition to XRD, which measures long-range atomic order in crystals, we observed
613 that the spin transition in synthetic $FeCO_3$ is a transient process that takes place over a
614 finite range of pressure under quasi-hydrostatic conditions. Moreover, our results
615 demonstrate that spin crossover is a dynamic process during which the Fe atoms in
616 HS and LS states coexist until the LS configuration is fully reached. A static
617 distribution of the two spin states can be excluded based on previous XRD studies
618 that reported only a sudden collapse of unit cell volume, but no other ordering
619 features.
620 The calculated Grüneisen parameters for all observed Raman modes agree with
621 the structural arrangement for $FeCO_3$ in HS and LS states reported previously in
622 single crystal XRD studies. While the CO_3 groups are relatively incompressible over
623 the entire pressure range investigated, Fe-O octahedra show a drastic change in their
624 stiffness after spin crossover, becoming more compact and hence harder to compress.
625 Deviatoric stress, both macroscopic and microscopic, causes remarkable
626 changes in the high-pressure behavior of $FeCO_3$. Local distortions of the Fe site cause
627 spin crossover to start at higher pressure and a broadening of the spin transition
628 pressure range.
629 Our results contribute to understanding the fate of iron-bearing carbonates
630 during subduction. Our experiments clearly show that deformation, which in the Earth
631 is caused by differential stress in the matrix due to processes such as convection,
632 increases the depth at which spin crossover starts and broadens its pressure range
633 beyond 5 GPa. This conclusion is valid both for our room temperature experiments as
634 well as for mantle conditions. Combined with the results of Liu et al. (2014) who
635 demonstrated that temperature extends the spin crossover region to higher pressure,
636 spin crossover in magnesiosiderite would start at much greater depths (> 150 km)
637 than postulated so far in previous work (e.g., Lavina et al., 2009), and would be
638 prolonged over a depth range of at least 300-350 km instead of being a sharp
639 discontinuity in the shallower part of the lower mantle. However, further experiments

640 are required in order to quantify more precisely the effect of temperature on natural
641 systems under the influence of deviatoric stress.
642
643 **References**
644
645 Bianconi, A., Dell'Ariccia, M., Gargano, A., and Natoli, C.R. (1983) Bond length
646 determination using XANES. In A. Bianconi, L. Incoccia, and S. Stilpcich, Eds.,
647 EXAFS and Near Edge Structure, 27, p. 57-61. Springer Series in Chemistry and
648 Physics, Berlin.
649
650 Biellmann, C., Gillet, P., Guyot, F., Peyronneau, J., and Reynard, B. (1993)
651 Experimental evidence for carbonate stability in the Earth's lower mantle. Earth and
652 Planetary Science Letters, 118, 31-41.
653
654 Boulard, E., Menguy, N., Auzende, A.L., Benzerara, K., Bureau, H., Antonangeli, D.,
655 Corgne, A., Morard, G., Siebert, J., Perrillat, J.P., Guyot, F., and Fiquet, G. (2012)
656 Experimental investigation of the stability of Fe-rich carbonates in the lower mantle.
657 Journal of Geophysical Research, 117, B02208.
658
659 Brenker, F.E., Vollmer, C., Vincze, L., Vekemans, B., Szymansky, A., Janssens, K.,
660 Szaloki, I., Nasdala, L., Joswig, W., and Kaminsky, F. (2007) Carbonates from the
661 lower part of the transition zone or even the lower mantle. Earth and Planetary
662 Science Letters, 260, 1-9.
663
664 Caliebe, W.A., Kao, C.C., Hastings, J.B., Taguchi, M., Kotani, A., Uozumi, T., and
665 de Groot, F.M.F. (1998) 1s2p resonant inelastic x-ray scattering in γ-Fe_2O_3. Physical
666 Review B, 58, 13452-13458.
667
668 Dasgupta, R. and Hirschmann, M.M. (2010) The deep carbon cycle and melting in
669 Earth's interior. Earth and Planetary Science Letters, 298, 1-13.
670
671 Dubrovinsky, L., and Dubrovinskaia, N. (2004) Angle-dispersive diffraction under
672 non-hydrostatic stress in diamond anvil cells. Journal of Alloys and Compounds, 375,
673 86-92.

Farfan, G., Wang, S., Ma, H., Caracas, R., and Mao, W.L. Bonding and structural changes in siderite at high pressure (2012). American Mineralogist, 97, 1421-1427.

Franzolin, E., Schmidt, M.W., and Poli, S. (2011) Ternary Ca-Fe-Mg carbonates: subsolidus phase relations at 3.5 GPa and a thermodynamic solid solution model including order/disorder. Contributions to Mineralogy and Petrology, 161, 213-227.

French, B.M. (1971) Stability relations of siderite ($FeCO_3$) in the system Fe-C-O. American Journal of Science, 27, pp. 37 -78.

Fukao, Y., Obayashi, M., and Nakakuki, T. (2009) Stagnant Slab: A Review. Annual Review of Earth and Planetary Science, 37, 19.

Goldsmith, J.R., Graf, D.L., Witters, J., and Northrop, D.A. (1962) Dolomite-Magnesian calcite relations at elevated temperature and CO_2 pressures. Geochimica et Cosmochimica Acta, 7(3-4), 109-128.

Gütlich, P. (1978) Mössbauer spectroscopy and transition metal chemistry. Berlin, Heidelberg: Springer-Verlag.

Harte, B. (2011) Diamond Window into the Lower Mantle. Science, 334, 51-52.

Isshiki, M., Irifune, T., Hirose, K., Ono, S., Ohishi, Y., Watanuki, T., Nishibori, E., Takata, M., and Sakata, M. (2004) Stability of magnesite and its high-pressure form in the lowermost mantle. Nature, 427, 60-63.

Kantor, I., Dubrovinsky, L., McCammon, C., Kantor, A., Pascarelli, S., Aquilanti, G., Crichton, W., M., R., Almeida, J., and Urusov, V. (2006a) Pressure-induced phase transition in $Mg_{0.80}Fe_{0.20}O$ ferropericlase. Physics and Chemistry of Minerals, 33, 35-44.

706 Kantor, I. Yu., Dubrovinsky, L. S., and McCammon, C. (2006b) Spin crossover in
707 (Mg,Fe)O: A Mössbauer effect study with an alternative interpretation of x-ray
708 emission spectroscopy data. Physical Review B, 73, 100101(R).
709
710 Kantor, I. (2007) High-pressure and high-temperature structural and electronic
711 properties of (Mg,Fe)O and FeO. 150 p. Ph.D Thesis, University of Bayreuth,
712 Bayreuth.
713
714 Kantor, I. Yu., Prakapenka, V., Kantor, A., Dera, P., Kurnosov, A., Sinogeikin, S.,
715 Dubrovinskaia, N., and Dubrovinsky, L. (2012) BX90: A new diamond anvil cell
716 design for X-ray diffraction and optical measurements. Review of Scientific
717 Instruments, 83, 125102.
718
719 Keppler, H., Wiedenbeck, M., and Shcheka, S.S. (2003) Carbon solubility in olivine
720 and the mode of carbon storage in the Earth's mantle. Nature, 242, 414-416.
721
722 Kurnosov, A., Kantor, I., Boffa-Ballaran, T., Lindhardt, S., Dubrovisnky, L.,
723 Kuznetsov, A., and Zehnder, B.H. (2008) A novel gas-loading system for
724 mechanically closing of various types of diamond anvil cells. Review of Scientific
725 Instruments, 79, 045110.
726
727 Lavina B., Dera P., Downs R.T., Prakapenka V., Rivers M., Sutton S., and Nicol M.
728 (2009) Siderite at lower mantle conditions and the effects of the pressure-induced
729 spin-pairing transition. Geophysical Research Letters, 36, L23306.
730
731 Lavina, B., Dera, P., Downs, R. T., Yang, W., Sinogeikin, S., Meng, Y., Shenand, G.,
732 and Schiferl, D. (2010a) Structure of siderite FeCO3 to 56 GPa and hysteresis of its
733 spin-pairing transition. Physical Review B, 82, 064110.
734
735 Lavina, B., Dera, P., Downs, R. T., Tschauner, O., Yang, W., Shebanova, O., and
736 Shen, G. (2010b) Effect of dilution on the spin pairing transition in rhombohedral
737 carbonates. High Pressure Research, 30, 224-229.
738

739 Lin, J.F., Liu, J., Jacobs, C., and Prakapenka, V.B. (2012b) Vibrational and elastic
740 properties of ferromagnesite across the electronic spin-pairing transition of iron.
741 American Mineralogist, 97, 583-591.
742
743 Liu, J., Lin, J.F., Mao, Z., and Prakapenka, V.B. (2014) Thermal equation of state and
744 spin transition of magnesiosiderite at high pressure and temperature. American
745 Mineralogist, 99, 84-93.
746
747 Liu, J., Lin, J.-F., and Prakapenka, V.B. (2015) High-pressure orthorhombic
748 ferromagnesite as a potential deep-mantle carbon carrier. Scientific Reports, 5, 7640,
749 doi: 10.1038/srep07640..
750
751 Mao, H.K., Xu, J., and Bell, P.M. (1986) Calibration of the ruby pressure gauge to
752 800 kbar under quasi-hydrostatic conditions. Journal of Geophysical Research, 91,
753 4673.
754
755 Mao, Z., Armentrout, M., Rainey, E., Manning, C.E., and Dera, P. (2011) Dolomite
756 III: A new candidate lower mantle carbonate. Geophysical Research Letters, 38,
757 L22303.
758
759 Mattila, A., Pylkkänen, T., Rueff, J.P., Huotari, S., Vankó, G., Hanfland, M.,
760 Lehtinen, M., and Hämäläinen K. (2007) Pressure induced magnetic transition in
761 siderite $FeCO_3$ studied by x-ray emission spectroscopy. Journal of Physics:
762 Condensed Matter, 19, 38, 386206.
763
764 McCammon, C., Dubrovinsky, L., Narygina, O., Kantor, I., Wu, X., Glazyrin, K.,
765 Sergueev, I., and Chumakov, A.I. (2010) Low-spin Fe^{2+} in silicate perovskite and a
766 possible layer at the base of the lower mantle. Physics of the Earth and Planetary
767 Interiors, 180, 215-221.
768
769 Meng, Y., Weidner, D.J., and Fei, Y. (1993) Deviatoric stress in a quasi-hydrostatic
770 diamond anvil cell: Effect on the volume-based pressure calibration. Geophysical
771 Research Letters, 20, 1147-1150.
772

773 Merlini, M., Crichton, W.A., Hanfland, M., Gemmi, M., Mueller, H., Kupenko, I.,
774 and Dubrovinsky, L. (2012) Structures of dolomite at ultrahigh pressure and their
775 influence on the deep carbon cycle. Proceedings of the National Academy of
776 Sciences, 109, 13509-13514.
777
778 Merlini, M., and Hanfland, M. (2013) Single-crystal diffraction at megabar conditions
779 by synchrotron radiation. High Pressure Research: an International Journal, 33, 511-
780 522.
781
782 Merrill, L., and Basset, W.A. (1975) The crystal structure of $CaCO_3$-(II), a high-
783 pressure metastable phase of calcium carbonate. Acta Cryst., B31, 343-349.
784
785 Mottana, A. (2004) X-ray absorption spectroscopy in mineralogy: Theory and
786 experiment in the XANES region. EMU Notes in Mineralogy, 6, 465-552.
787
788 Narygina, O., Mattesini, M., Kantor, I., Pascarelli, S., Wu, X., Aquilanti, G.,
789 McCammon, C., and Dubrovinsky, L. (2009) High-pressure experimental and
790 computational XANES studies of $(Mg,Fe)(Si,Al)O_3$ perovskite and (Mg,Fe)O
791 ferropericlase as in the Earth's lower mantle. Physical Review B, 79, 174115.
792
793 Ono, S., Kikegawa, T., Ohishi, Y., and Tsuchya, J. (2005) Post-aragonite phase
794 transformation in CaCO3 at 40 GPa. American Mineralogist, 90, 667-671.
795
796 Pascarelli, S., Mathon, O., Muñoz, M., Mairs, T., and Susini J. (2006) Energy-
797 dispersive absorption spectroscopy for hard-X-ray micro-XAS applications. Journal
798 of Synchrotron Radiation, 13, 351-358.
799
800 Popkov, Yu. A., Eremenko, V.V., Fomin, V.I., and Mokhir, A.P. (1973) Raman
801 scattering of light in antiferromagnetic siderite. Soviet Physics - Solid State, 14, 1985-
802 1989.
803
804 Potapkin, V., Chumakov, A.I., Smirnov, G.V., Celse, J.P., Rüffer, R., McCammon,
805 C., and Dubrovinsky, L. (2012) The ^{57}Fe Synchrotron Mössbauer Source at the ESRF.
806 Journal of Synchrotron Radiation, 19, 559-569.

Prescher, C., McCammon, C., and Dubrovisnky, L. (2012a) MossA: a program for analyzing energy-domain Mössbauer spectra from conventional and synchrotron sources. Journal of Applied Crystallography, 45, 329-331.

Prescher, C., Dubrovinsky, L., McCammon, C., Glazyrin, K., Nakajima, Y., Kantor, A., Merlini, M., and Hanfland, M. (2012b) Structurally hidden magnetic transitions in Fe3C at high pressures. Physical Review B, 85, 140402.

Ravel, B., and Newville, M. (2005) ATHENA, ARTEMIS, HEPHAESTUS: data analysis for X-ray absorption spectroscopy using IFEFFIT. Journal of synchrotron radiation, 12, 537–41.

Rosenberg, P. E. (1967) Subsolidus relations in system $CaCO_3$-$MgCO_3$-$FeCO_3$ between 350° and 500° C. American Mineralogist, 52, 787-796.

Ross, N.L., and Reeder, R.J. (1992) High –pressure structural study of dolomite and ankerite. American Mineralogist, 77, 412-421.

Rüffer, R., and Chumakov, A.I. (1996) Nuclear Resonance Beamline at ESRF. Hyperfine Interactions, 97/98, 589-604.

Rutt, H.N., and Nicola, J.H. (1974) Raman spectra of carbonates of calcite structure. Journal of Physics C: Solid State Physics, 7, 4522.

Santillán, J., and Williams, Q. (2004) A high-pressure infrared and X-ray study of $FeCO_3$ and $MnCO_3$: comparison with $CaMg(CO_3)_2$-dolomite. Physics of the Earth and Planetary Interiors, 143-144, 291-304.

Shi, H., Luo, W. Johansson, B., and Ahuja, R. (2008) First-principles calculations of the electronic structure and pressure-induced magnetic transition in siderite $FeCO_3$. Physical Review B, 78, 155119.

Stagno, V., Tange, Y., Miyajima, N., McCammon, C.A., Irifune, T., and Frost, D.J. (2011) The stability of magnesite in the transition zone and lower mantle as function of oxygen fugacity. Geophysical Research Letters, 38, L19309.

Sturhahn, W., Jackson, J. M., and Lin, J.F. (2005) The spin state of iron in minerals of Earth's lower mantle. Geophysical Research Letters, 32, 1-5.

Takemura, K. (2001) Evaluation of the hydrostaticity of a helium-pressure medium with powder x-ray diffraction techniques. Journal of Applied Physics, 89, 662, DOI: 10.1063/1.1328410.

Walter, M.J., Kohn, S.C., Araujo, D., Bulanova, G.P., Smith, C.B., Gaillou, E., Wang, J., Steele, A., and Shirey, S.B. (2011) Deep Mantle Cycling of Oceanic Crust: Evidence from Diamonds and Their Mineral Inclusions. Science, 334, 54-57.

Weidner, D.J., Wang, Y., and Vaughan, M.T. (1994) Yield strength at high pressure and temperature. Geophysical Research Letters, 21, 753-756.

Westre, T. E., Kennepohl, P., DeWitt, J. G., Hedman, B., Hodgson, K. O., and Solomon, O. E. (1997) A Multiplet Analysis of Fe K-Edge 1s → 3d Pre-Edge Features of Iron Complexes. Journal of the American Chemical Society, 119, 6297-6314.

Wilke, M., Farges, F., Petit, P. E., Brown, Jr. G. E., and Martin, F. (2001) Oxidation state and coordination of Fe in minerals: an Fe K XANES spectroscopic study. American Mineralogist, 86, 714-730.

Wilke, M., Farges, F., Partzsch, G.M., Schmidt, C., and Behrens, H. (2007) Speciation of iron in silicate glasses and melts by in-situ XANES spectroscopy. American Mineralogist, 92, 44-56.

Wood, B. J. (1993) Carbon in the Core. Earth and Planetary Science Letters, 117, 593-607.

Zhao, J., Angel, R.J., and Ross N.L. (2010) Effects of deviatoric stresses in diamonds-anvil cell on single-crystal samples. Journal of Applied Crystallography, 43, 743-751.

Zhang, J., and Reeder, R.J. (1999). Comparative compressibilities of calcite-structure carbonates: deviations from empirical relations. American Mineralogist, 84, 861–870.

Figure captions

Figure 1. Photographs of $FeCO_3$ samples in DACs at the indicated pressures with (a) one single crystal and (b) multiple single crystals, each surrounded by Ne. Both loadings contain a small ruby crystal as a pressure calibrant.

Figure 2. Room temperature Mössbauer spectra of $FeCO_3$ (a) single crystals and (c) powder collected in house at the indicated pressures. (b) SMS spectra of one $FeCO_3$ single crystal collected at ESRF, Grenoble (France). Solid circles: experimental data; black lines: full transmission integral fit; blue and red lines: individual subspectra. Note that the subspectra do not add up to the total spectrum due to the properties of the full transmission integral fit. Percentage bars indicate the relative absorption.

Figure 3. Room temperature centre shift (a) and quadrupole splitting (b) (relative to α-Fe) of $FeCO_3$ as a function of pressure. Solid circles: in house single crystals experiments; open circles: in house powder experiment; solid triangles: SMS single crystal experiment.

Figure 4. Comparison of room temperature $FeCO_3$ Mössbauer spectra: (a) SMS collected on one single crystal at 19 GPa; (b) in house collected on multiple single crystals at 18 GPa; and (c) in house collected on powder at 20.5 GPa. The area asymmetry of the doublet in (a) is due to polarization of the synchrotron Mössbauer source. Percentage bars indicate the relative absorption.

Figure 5. Effect of pressure on the full-width at half-maximum (FWHM) of $FeCO_3$ spectra. Open circles: in house powder; solid circles: in house single crystals; solid triangles: SMS single crystal. Dashed lines indicate the pressure at which spin crossover starts for single crystal (41 GPa) and powder (52 GPa) measurements.

Figure 6. Raman spectra of $FeCO_3$ collected at ambient temperature and the indicated pressures. The two modes below 500 cm^{-1} are external or lattice vibrations of CO_3^{2-} relative to Fe atoms, while modes above 700 cm^{-1} are internal vibrations of CO_3^{2-}. The insets indicate the lower frequency Raman bands for the spectra on a different scale.

Figure 7. Pressure variation of the peak shift of observed Raman modes of $FeCO_3$. Dashed grey area indicates the spin crossover pressure range. The frequency uncertainty is smaller than the size of the symbols.

Figure 8. Pressure variation of Raman mode intensity normalized to the most intense mode, A_{1g}, in $FeCO_3$. Solid circles: lower frequency external E_g vibration; open circles: higher frequency external E_g vibration; solid triangles: internal E_g vibration (see also Figs. 7 and 8). Note that the lowest frequency external E_g mode disappears completely above 45 GPa.

Figure 9. (a) Normalized XAS spectra of $FeCO_3$ at room temperature collected on compression at the indicated pressures. The inset at the bottom right highlights the pre-edge region of the 1 bar spectrum. (b) Close up on the evolution of the pre-edge region with pressure. The spectra are shifted vertically for clarity.

Figure 10. Pressure variation of maximum peak positions for $FeCO_3$ XANES spectra. The peaks are labeled according to Fig. 9 and the grey dashed area indicates where the transition is observed in the XANES spectra.

Figure 11. $\delta\mu/\delta E$ derivatives of room temperature XANES spectra of $FeCO_3$ at the indicated pressures. The vertical unit is arbitrary, and the derivatives are taken from the normalized spectra (Fig. 10). Grey arrows and dashed lines indicate the energies at which changes are observed at 44 GPa.

Figure 12. Pressure variation of the intensity ratio (I1/I2) of the main peaks (see Fig. 9) of $FeCO_3$ XANES spectra. The percentage change at the transition pressure is indicated.

Figures

Figure 1

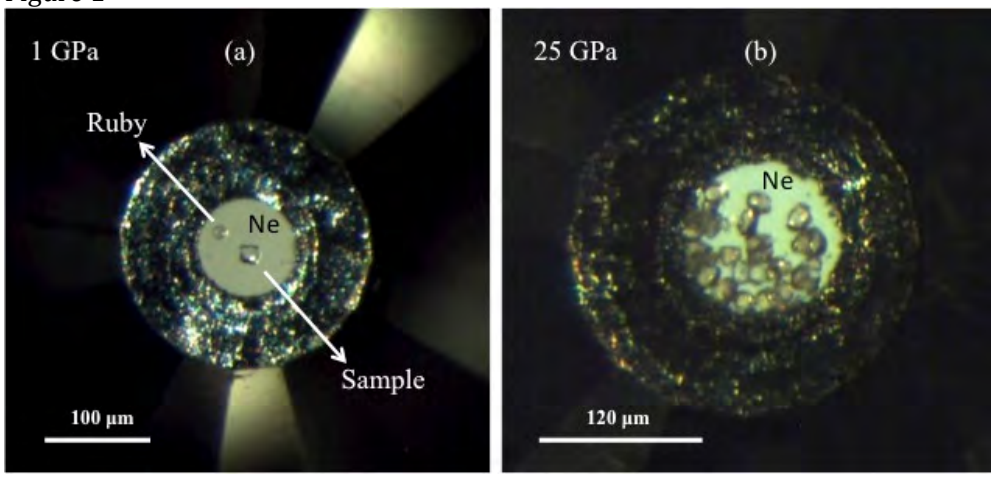

Figure 2

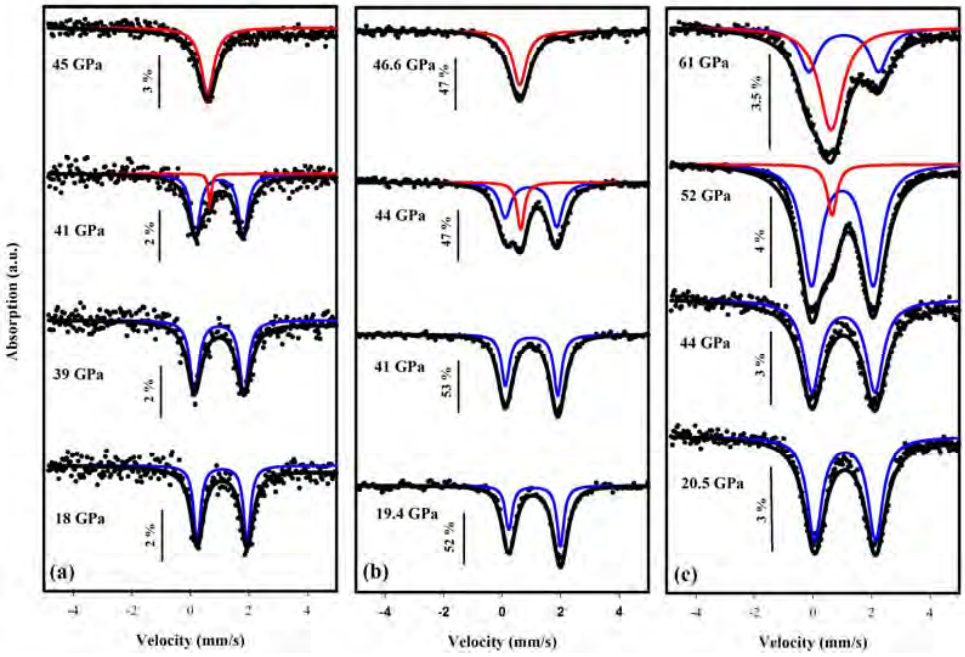

Figure 3

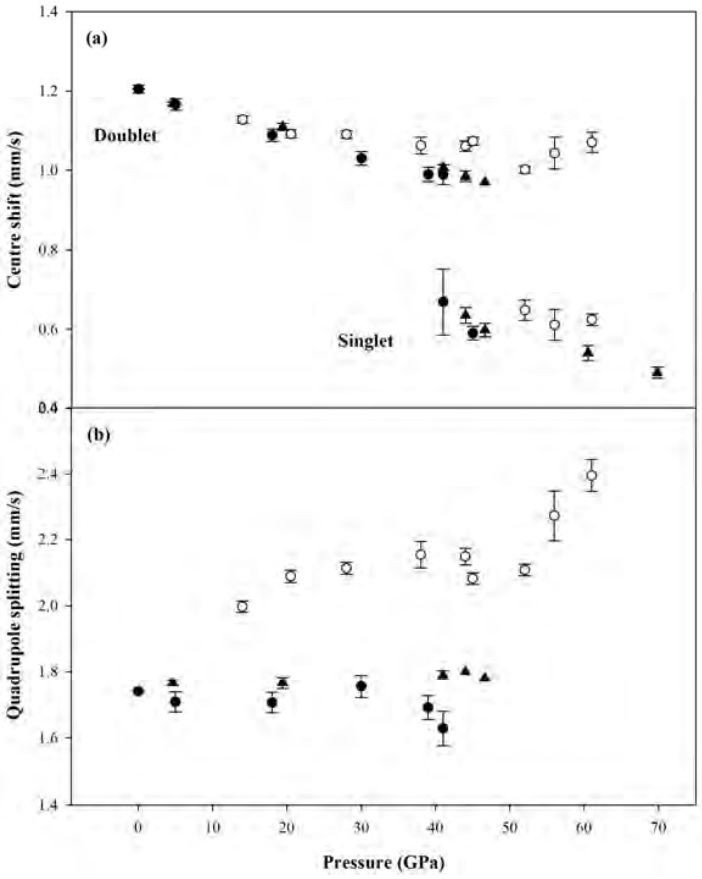

Figure 4

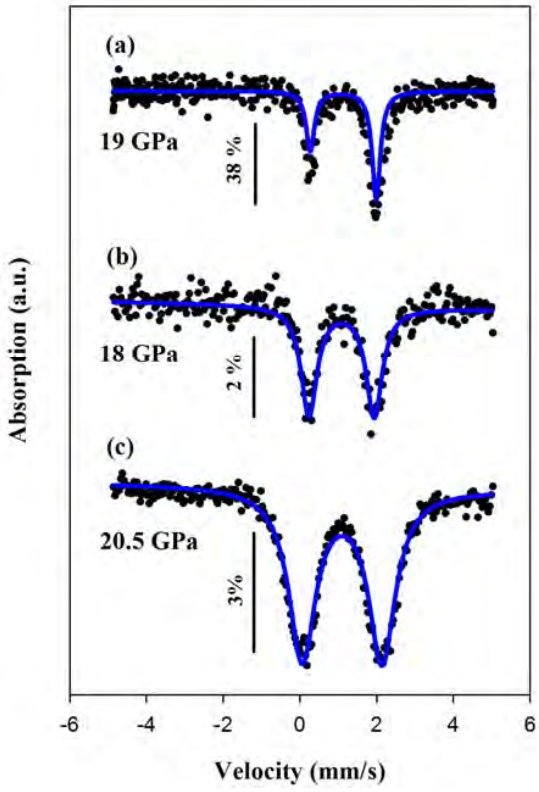

Figure 5

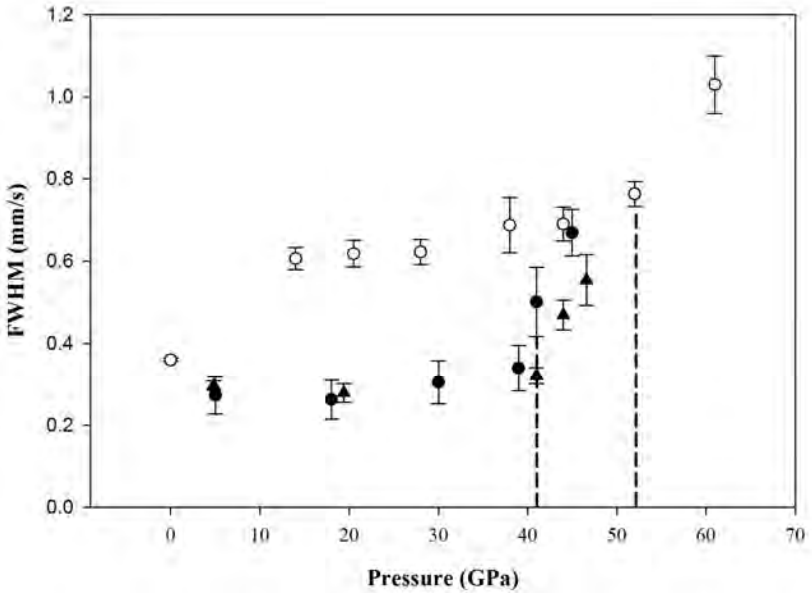

Figure 6

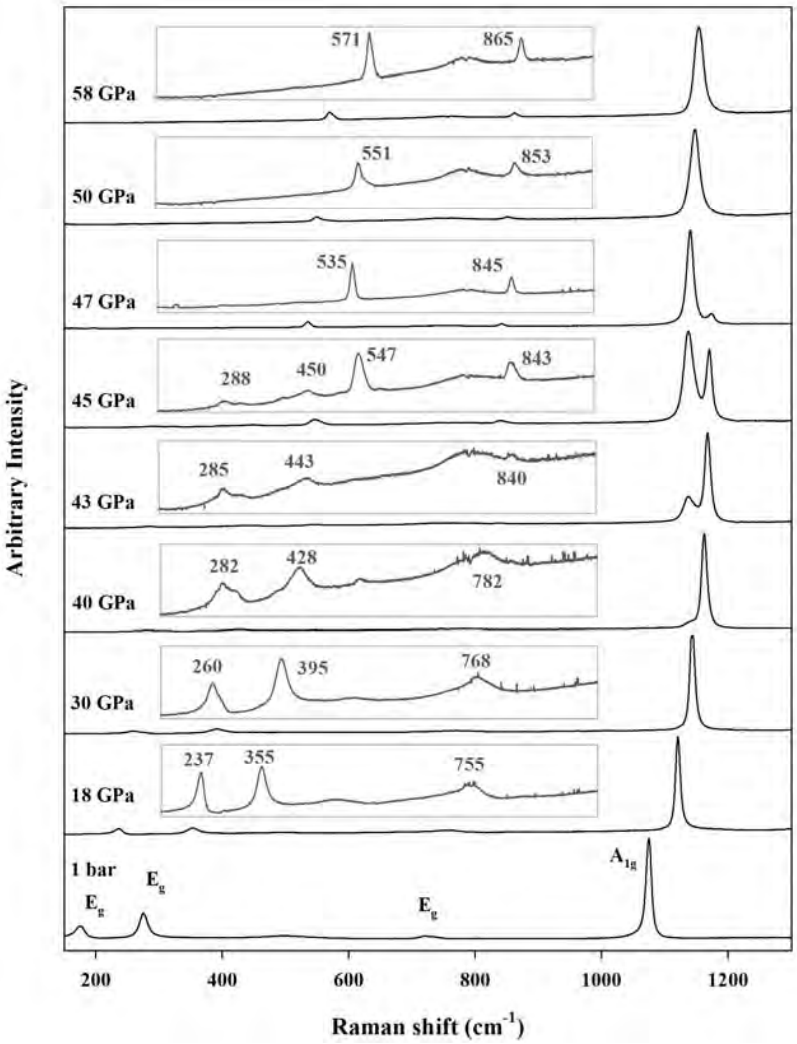

1030
1031
1032 Figure 7

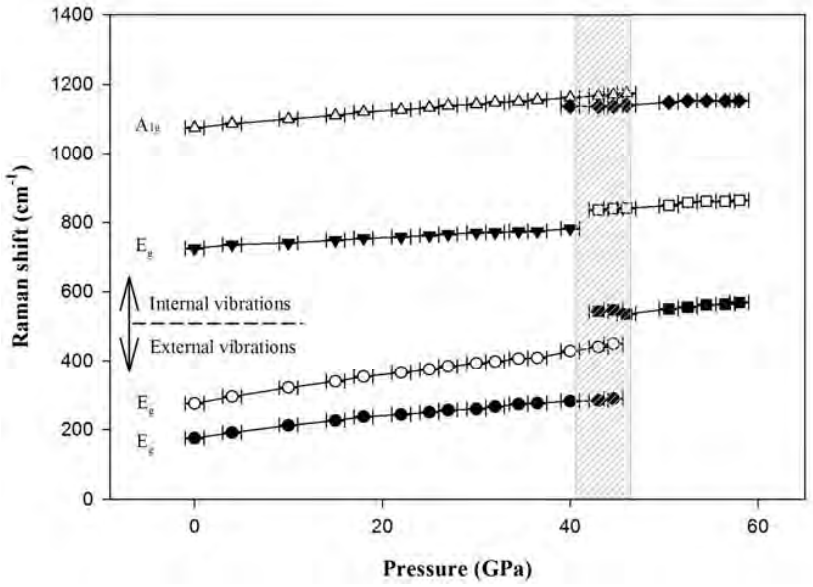

1033
1034
1035 Figure 8

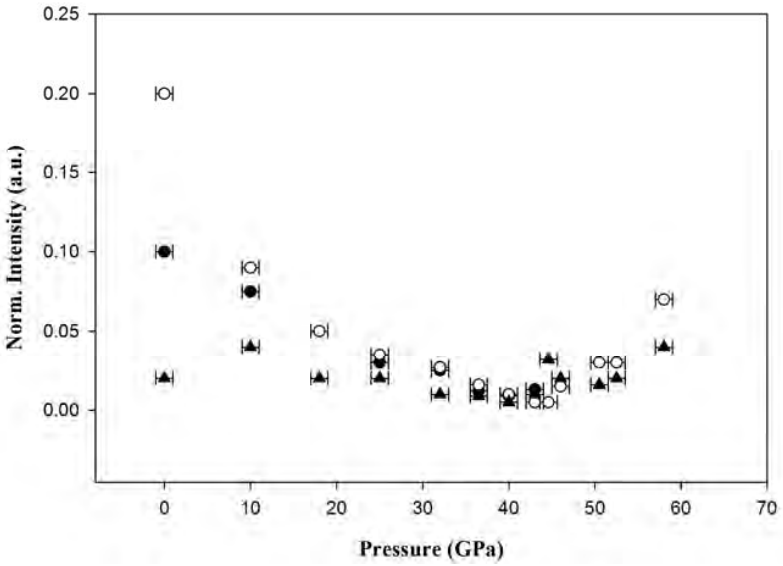

1036
1037
1038
1039
1040

Figure 9

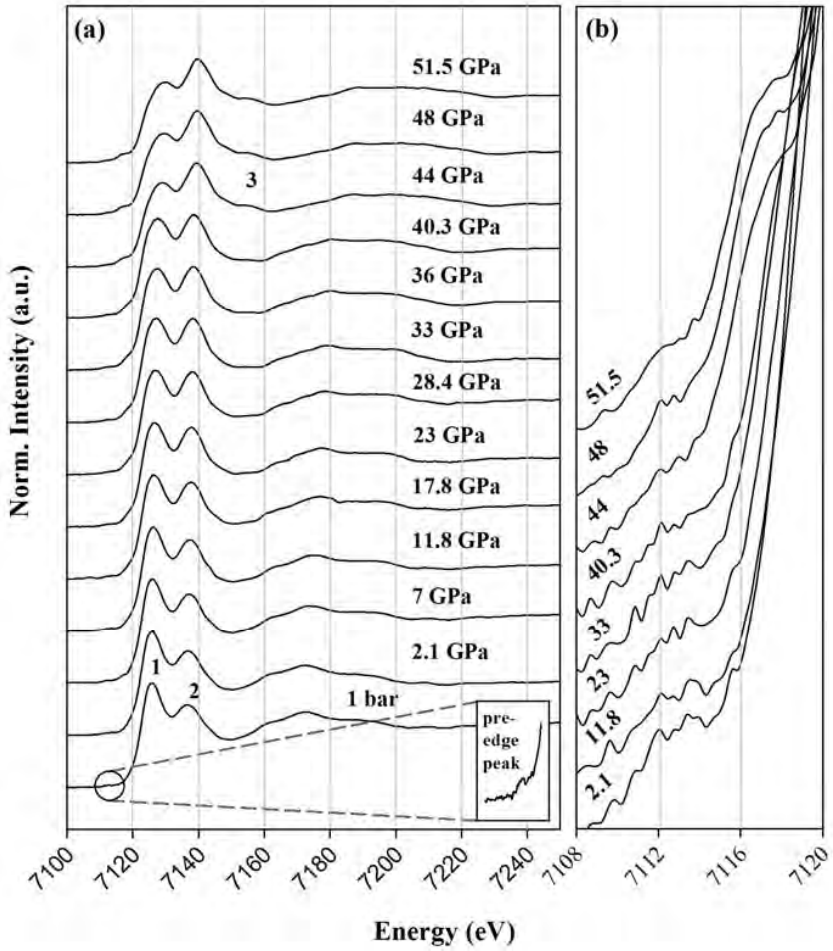

Figure 10

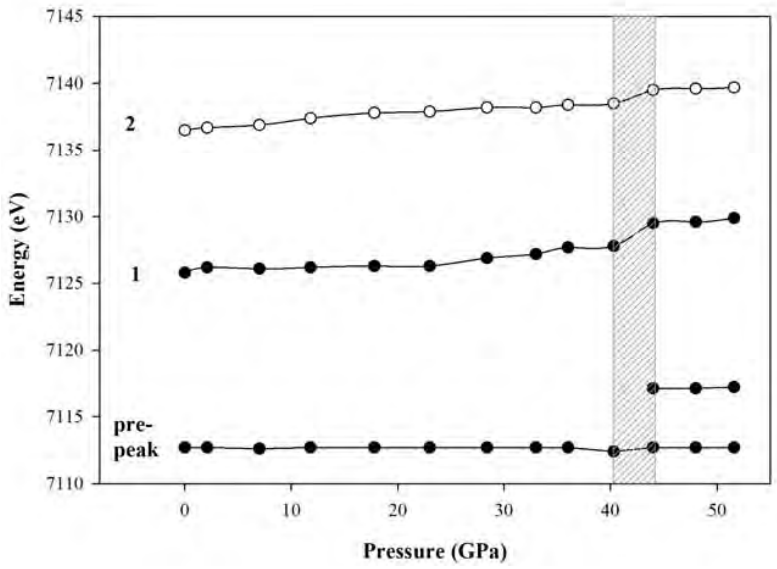

Figure 11

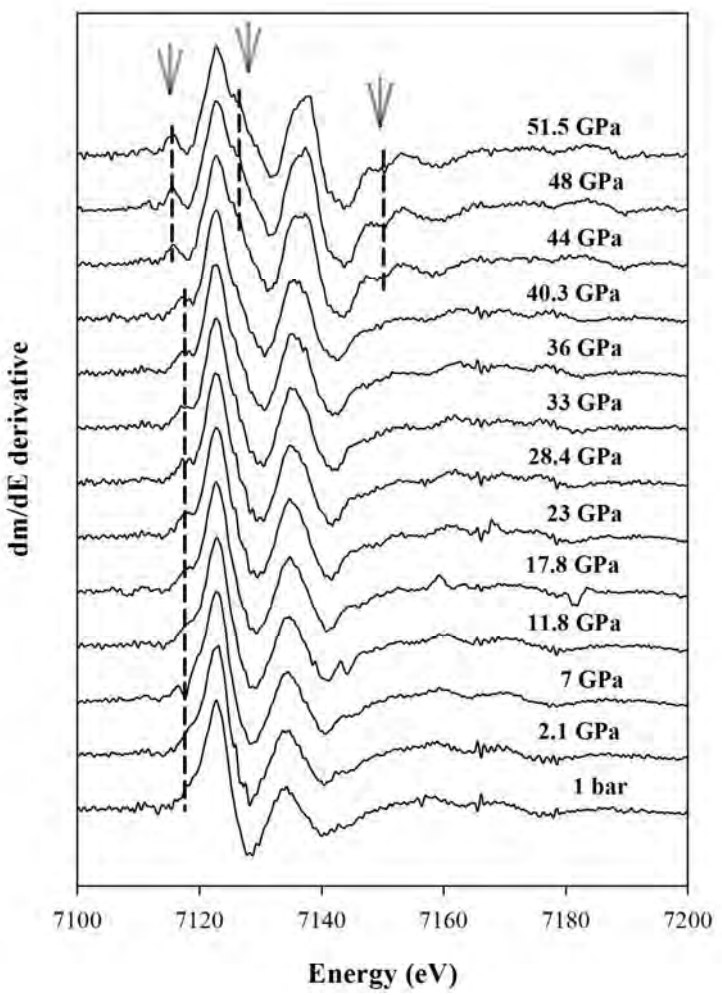

Figure 12

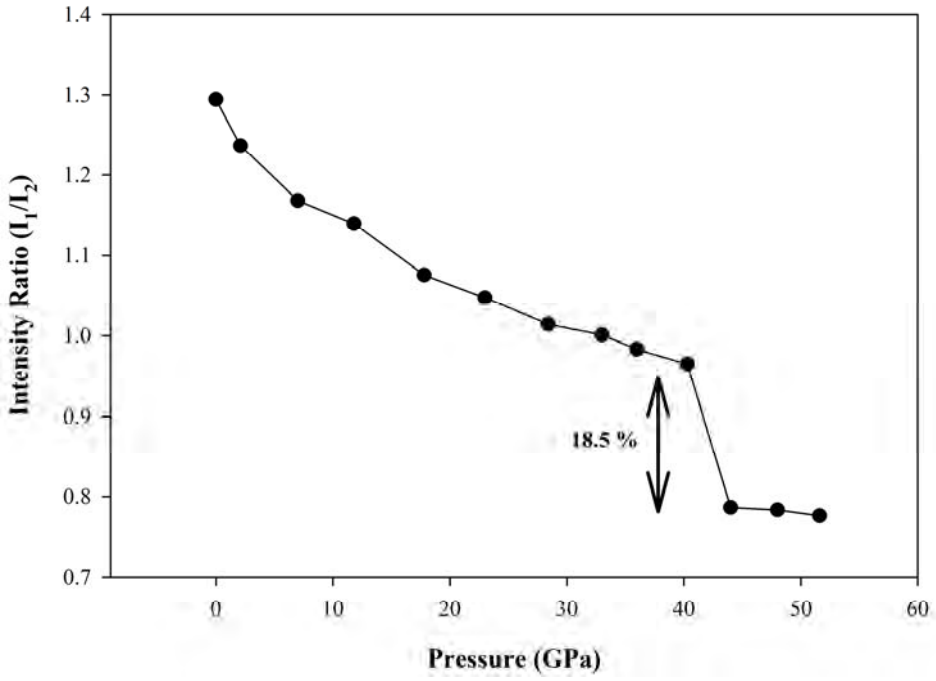

Tables

Table 1

Grüneisen parameter (γ_i) for Raman vibrational modes

Modes	Assignment	dω/dP ($cm^{-1}GPa^{-1}$)		Mean mode γ_i	
		HS	LS	HS	LS
A_{1g} (internal)	Symmetric (in plane) stretching	2.17	1.6	0.22	0.21
E_g (internal)	Symmetric (in plane) bending	1.37	1.86	0.21	0.32
E_g (external)	Translatory oscillations of the CO_3 groups	3.82	2.68	1.16	0.72
E_g (external)		2.51		1.18	
Mean mode Grüneisen parameter for observed vibrational mode in HS state:					0.69
Mean mode Grüneisen parameter for observed vibrational mode in LS state:					0.42

Bulk moduli from Zhang and Reeder (1998) and Lavina et al. (2010) for HS and LS configuration respectively.
Band assignments from Rutt and Nicola (1974).